

A TECHNICAL DESCRIPTION OF ATMOSPHERIC SOUNDING BY GPS OCCULTATION

G. A. Hajj, E. R. Kursinski, L. J. Romans, W. I. Bertiger, S. S. Leroy
Jet Propulsion Laboratory

ABSTRACT

In recent years, the Global Positioning System (GPS) has been exploited via radio occultation techniques to obtain profiles of refractivity, temperature, pressure and water vapor in the neutral atmosphere and electron density in the ionosphere. The GPS/MET experiment, which placed a GPS receiver in a low-Earth orbit, provided a wealth of data which was used to test this concept and the accuracy of the retrievals. Several investigations have already demonstrated that the retrieval accuracies obtained with GPS/MET is already comparable, if not better, than the more traditional atmospheric sensing techniques (e.g., radiosondes). Even though the concept of atmospheric profiling via radio occultation is quite a simple one, care must be taken to separate the numerous factors that can affect the occulted signal. These include the motion of the satellites, clock drifts, relativistic effects, the separation of the ionosphere and the neutral atmosphere, and the contribution of the upper atmosphere where sensitivity of the GPS signal is weak. In addition, care must be taken to use proper boundary conditions, use proper smoothing intervals and interpolation schemes to avoid retrieving artificial atmospheric structures, and most importantly detect and correct phase measurement errors introduced by sharp refractivity gradients in the atmosphere. This work describes in some detail the several steps involved in processing such data. In particular, it describes a system that was developed at the Jet Propulsion Laboratory and used to process the GPS/MET data. Several examples of retrieved refractivity, temperature and water vapor profiles are shown and compared to analyses from the European Center for Medium-range Weather Forecast (ECMWF). Statistical comparisons of GPS/MET and ECMWF temperatures for data collected during June 21-July 4, 1995, indicate that differences are of order 1-2K at northern latitudes where the ECMWF analyses are most accurate.

1. INTRODUCTION

The radio occultation technique has three decades of history as a part of NASA's planetary exploration missions [e.g., *Fjeldbo and Eshleman*, 1969; *Fjeldbo et al.*, 1971; *Tyler*, 1987; *Lindal et al.*, 1990; *Lindal*, 1992]. Applying the technique to the Earth's atmosphere using the Global Positioning System (GPS) signal was conceived a decade ago [e.g., *Yunck et al.*, 1988; *Gurvich and Krasil'nikova*, 1990] and demonstrated for the first time with the GPS/MET experiment in 1995 [*Ware et al.*, 1996]. The promises of the technique have generated much interest from several disciplines including meteorology, climatology and ionospheric physics.

The technique relies on very accurate measurements of the GPS dual-frequency phase delays collected from a receiver in low-Earth orbit (LEO) tracking a GPS satellite setting or rising behind the Earth's atmosphere. The extra phase delay induced by the atmosphere can be converted to atmospheric bending which can then be interpreted in terms of refraction due to atmospheric refractivity changes at different heights. Assuming spherical symmetry in the locality of the occulting atmosphere, the index of refraction can therefore be determined from the height of the LEO down to the Earth's surface. Index of refraction can then be converted into electron density above 60 km, neutral atmospheric density, pressure and temperature between 60 km and the middle troposphere, and, with

independent knowledge of temperature, into water vapor density in the middle and lower troposphere.

Numerous articles and reports have been written describing the technique, its resolution and accuracy, and its relevance to climate, weather and ionospheric research. On the theoretical front, several papers have addressed the expected resolution and accuracy of the technique [e.g., *Gorbunov and Sokolovskiy*, 1993; *Hajj et al.*, 1994; *Melbourne et al.*, 1994; *Kursinski et al.*, 1995; *Hoeg et al.*, 1995; *Gorbunov*, 1996; *Gorbunov et al.*, 1996a; *Kursinski et al.*, 1997]. On the observational front, GPS/MET data have been used to derive temperature, water vapor, geopotential heights of constant pressure levels and ionospheric electron density profiles. GPS/MET-derived temperature profiles agree with those from radiosondes and analyses from the European Center for Medium-range Weather Forecast (ECMWF) to better than 1.5K between 5 and 30 km altitudes [*Hajj et al.*, 1995; *Kursinski et al.*, 1996; *Ware et al.*, 1996; *Rocken et al.*, 1997; *Steiner et al.*, 1999]. GPS/MET-derived geopotential heights of constant pressure levels agree with those of the ECMWF to ~20 gpm [*Leroy*, 1997]. GPS/MET-derived specific humidities agree with those of the ECMWF to ~0.1 g/kg in the mean [*Kursinski and Hajj*, 1999]. In the ionosphere, GPS/MET data were analyzed to derive electron density profiles in the E and F regions [*Hajj and Romans*, 1998; *Schreiner et al.*, 1999] and peak electron densities were shown to agree with those of digisondes at the 20% level ($1-\sigma$). In addition, tomographic inversions of GPS/MET data were performed to obtain 2-dimensional (2-D) and 3-D images of electron density [*Hajj et al.*, 1996; *Rius et al.*, 1998].

Other studies have considered the use of GPS occultation products (e.g. atmospheric delay or profiles of refractivity) in applications such as climate change detection [*Yuan et al.*, 1993] and numerical weather predictions [*Eyre*, 1994; *Zou et al.*, 1995; *Kuo et al.*, 1998]. Yet others have examined techniques to improve the vertical resolution and accuracy of the GPS occultation technique by means of diffraction corrections [*Gorbunov et al.*, 1996b] and combining ground and space data for ionospheric tomography [*Leitinger et al.*, 1997].

The purpose of this paper is to describe in detail a system developed at the Jet Propulsion Laboratory (JPL) for processing GPS radio occultation data to obtain profiles of refractivity, pressure, temperature in the lower neutral atmosphere (below 50 km altitude), water vapor in the middle and lower troposphere, and electron density in the ionosphere. While the technique is conceptually rather simple, there are several issues to be carefully considered in optimally analyzing the data. These issues include the proper calibration of phase delays measured from GPS in order to isolate the atmospheric delay, the detection and correction of measurement errors such as data outages and cycle slips, the proper smoothing of the data and the associated measurement resolution, and the evaluation of errors associated with the estimated atmospheric delay, Doppler shift and bending. The processing steps are illustrated with a specific occultation. Other examples of retrieved refractivity, temperature and water vapor are discussed. Statistical comparisons of GPS/MET and ECMWF temperatures for data collected during June 21-July 5, 1995, are also shown.

The paper is structured as follows. In section 2 we describe the basics of the GPS signal and how it is modeled. Section 3 describes the process of extracting the atmospheric delay during an occultation and means of detecting and correcting measurement errors. Section 4 describes the inversion process which includes deriving the atmospheric induced Doppler shift and bending, removing the ionospheric effects, the Abel inversion, and then the derivation of the geophysical parameters from refractivity. In section 5 we present other examples of GPS/MET retrievals and comparisons to the ECMWF analyses. A conclusion is given in section 6.

2. GPS SIGNAL STRUCTURE AND OBSERVABLES

The GPS constellation consists of 24 satellites at ~26500 km radius, ~12hr period, orbiting in 6 different planes inclined at ~55°. Each GPS satellite broadcasts two signals at L-band ($f_1 = 1575.42$ Mhz and $f_2 = 1227.60$ MHz). The L1 and L2 signals received from each GPS satellite can be written as [Spilker, 1980]:

$$S_{L1}(t) = \sqrt{2C_{c/a}} D(t)X(t)\sin(2\pi f_1 t + \theta_1) + \sqrt{2C_{P1}} D(t)P(t)\cos(2\pi f_1 t + \theta_1) \quad (1)$$

$$S_{L2}(t) = \sqrt{2C_{P2}} D(t)P(t)\cos(2\pi f_2 t + \theta_2) \quad (2)$$

with

$C_{c/a}$, C_{P1} the received power of the in-phase and quadrature components of the L1 signal, respectively;

C_{P2} the received power of L2;

$D(t)$ an amplitude modulation for L1 and L2 containing navigation data;

$X(t)$ a pseudorandom sequence of ± 1 —known as clear acquisition or C/A code—modulating the in-phase component of L1 at a rate of 1.023 Mhz;

$P(t)$ a pseudorandom sequence of ± 1 —known as P-code—modulating the quadrature component of L1 and L2 at a rate of 10.23 Mhz.

A properly equipped receiver will detect amplitude, pseudorange¹ and phase measurements for each of the C/A, L1 P-code (P1) and L2 P-code (P2) signals. The C/A and P1 measurements essentially contain identical information, however C/A is preferred over P1 because its power is stronger by 3 dB and is not encrypted. Therefore, the basic observables used during an occultation experiment are the C/A phase and the P2 phase measurements between the low-Earth orbit (LEO) satellite and the occulting GPS satellite. These phase measurements can be modeled (in dimension of distance) as:

$$L_k^{ij} \equiv -\frac{c}{f_k} \Phi_k^{ij} = \rho^{ij} + \delta_k^{ij} + C^i + C^j + v_k \quad (3.a)$$

$$\delta_k^{ij} = \eta_k^{ij} + d \frac{TEC_k^{ij}}{f_k^2} \quad (3.b)$$

with

Φ_k^{ij} the recorded phase in cycles for the signal propagated from transmitter i to receiver j ;

c the speed of light in vacuum;

$k = 1$ or 2 for L1 and L2, respectively;

ρ^{ij} the range corresponding to the travel light time (in vacuum) between the transmitter and the receiver;

δ_k^{ij} the extra delay due to neutral atmosphere and ionosphere;

C^i, C^j time dependent transmitter and receiver clock errors, respectively;

v_k measurement noise which contains the receiver's thermal noise and local multipath.

η_k^{ij} the extra delay due to the neutral atmosphere;

¹ Pseudorange is an absolute measurement of group delay between the time a signal is transmitted and received. It is the sum of the actual range between the transmitter and the receiver, atmospheric and ionospheric delays and transmitter and receiver clocks offsets.

d a constant;
 TEC_k^{ij} the integrated electron density along the raypath;

Eq. (3.a) ignores the following terms:

(1) A bias corresponding to a large integer number of cycles which is constant over a connected arc (i.e., a GPS satellite tracked continuously during the occultation). It is the time derivative of the phase that is of interest to us during an occultation, therefore all additive constants can be ignored.

(2) The “wind-up” term that accounts for the relative orientation of the transmitting and the receiving antennas. Because the geometry and the relative orientation of the transmitting and receiving antennas are well known, this term is modeled and removed [Wu *et al.*, 1993].

(3) Transmitting and receiving antennas phase center variations (which can be calibrated if necessary).

Eq. (3.b) ignores higher order ionospheric terms (order $1/f^3$ or higher) which results from the expansion of the Appleton-Hartree formula [see, e.g., Bassiri and Hajj, 1994]. This term is normally small, but it becomes a dominant error term at high altitudes (> 40-60 km) during solar-maximum day-time conditions [Kursinski *et al.*, 1997].

Subscripts on any term in Eqs. (3.a-b) implies that it depends on the frequency. The neutral atmosphere is non-dispersive at radio frequencies; however, since the electromagnetic signal has to travel through the dispersive ionosphere before it arrives at the lower neutral atmosphere, the L1 and L2 signals received at a given time sense slightly different parts of the neutral atmosphere (as depicted by the solid, L1, and dotted, L2, occulted signals of Figure 1). This separation of L1 and L2 signals is the reason to have subscripts on the terms δ_k^{ij} and TEC_k^{ij} in Eq. (3.b).

3. ISOLATING ATMOSPHERIC DELAY

3.1 The Calibration Process

Isolating the extra delays induced by the Earth media, δ_k^{ij} and TEC_k^{ij} in Eq. (3.b), is the first necessary step toward reconstructing profiles of refractivity. This is accomplished by computing or modeling the clock terms on the right side of Eq. (3.a), a procedure that we refer to here as the calibration process.

Depending on the stability of the transmitter’s and receiver’s clocks, we may or may not need to solve for the clock terms in Eq. (3.a) (For the effects of clock instability on atmospheric retrievals, see Kursinski *et al.*, 1997). For the sake of generality, we will here assume that both the transmitter’s and the receiver’s clocks are sufficiently unstable and require calibration². In order to be able to solve for both the transmitter’s and receiver’s clocks, the following geometry is required (see Figure 1): An occulting receiver (LEO(4)) must view simultaneously an occulting transmitter (GPS(2)) and a non-occulting transmitter (GPS(3)). A second non-occulting receiver (GPS(1)) must simultaneously view both the GPS(2) and GPS(3). In order to understand how the calibration of the various clocks is performed we describe in some detail the modeling of the time delay.

We distinguish between three different types of time: (a) clock time, $\hat{\tau}$, which is the time recorded by the transmitter’s or receiver’s clock (we call time tag) and contains a time

² This is always true of the GPS clock when selective availability is turned on. It is also true of the GPS/MET receiver’s clock.

varying offset; (b) proper time, \bar{t} , which is the time recorded by a perfect clock in a frame moving with the transmitter or receiver; and (c) coordinate time, t , which is the time recorded by a perfect clock in a given coordinate system. A GPS receiver measures the range between the transmitter and the receiver by essentially differencing the transmitter's time tag associated with a given sequence of code from the receiver's time tag at the time that sequence is received. Up to a constant bias, phase measurements can be thought of in the same manner. Therefore, we can write

$$L^{21} = c(\hat{t}^1 - \hat{t}^2) = c\left\{\left(\hat{t}^1 - \bar{t}^1\right) + \left(\bar{t}^1 - t^1\right) + \left(t^1 - t^2\right) + \left(t^2 - \bar{t}^2\right) + \left(\bar{t}^2 - \hat{t}^2\right)\right\} \quad (4.a)$$

where 1 and 2 corresponds to the id's of the receiver and the transmitter, respectively, as shown in Figure 1. The difference between the received and transmit time is modeled as the sum of five terms on the right side of Eq. (4.a). In their respective order, these terms correspond to the following:

1-receiver's clock error

2-proper time - coordinate time at receiver (due to special and general relativistic effects)

3- light travel time

4- coordinate time - proper time at transmitter

5-transmitter's clock error.

Similarly for the other links of Figure (1) we can write

$$L^{31} = c(\hat{t}^1 - \hat{t}^3) = c\left\{\left(\hat{t}^1 - \bar{t}^1\right) + \left(\bar{t}^1 - t^1\right) + \left(t^1 - t^3\right) + \left(t^3 - \bar{t}^3\right) + \left(\bar{t}^3 - \hat{t}^3\right)\right\} \quad (4.b)$$

$$L^{24} = c(\hat{t}^4 - \hat{t}^2) = c\left\{\left(\hat{t}^4 - \bar{t}^4\right) + \left(\bar{t}^4 - t^4\right) + \left(t^4 - t^2\right) + \left(t^2 - \bar{t}^2\right) + \left(\bar{t}^2 - \hat{t}^2\right)\right\} \quad (4.c)$$

$$L^{34} = c(\hat{t}^4 - \hat{t}^3) = c\left\{\left(\hat{t}^4 - \bar{t}^4\right) + \left(\bar{t}^4 - t^4\right) + \left(t^4 - t^3\right) + \left(t^3 - \bar{t}^3\right) + \left(\bar{t}^3 - \hat{t}^3\right)\right\} \quad (4.d)$$

Under normal operation, for a given receiver time tag, the receiver will record the time delay from all tracked satellites. Therefore, in writing Eqs. (4), L^{21} and L^{31} have the same received time, and similarly for L^{24} and L^{34} ; but L^{21} and L^{24} have different transmit time (\bar{t}^2 and \bar{t}^2 , receptively), and similarly for L^{31} and L^{34} , in order to account for the difference in the travel light time. In an occultation geometry, the only term that is of interest to us is the light travel time associated with the L^{24} link, which includes the delay induced on the link by the atmosphere.

In order to obtain $t^4 - t^2$ we either solve for or compute all the other terms as follows:

(1) Based on knowledge of the positions of both transmitters and receivers (which are obtained from solutions of the orbit using a ground network of fiducials and all other GPS satellites), we solve for the light time associated with links L^{21} , L^{31} and L^{34} and for the time differences between coordinate and proper times for all links. This is done by accounting for special and general relativistic effects in the manner described by *Wu et al.*, 1990a and *Sovers and Border*, 1990. Eqs. (5)-(7) summarize their results which is applied to link L^{21} as an example:

The difference between proper time and coordinate time for a receiver fixed on the ground is given by

$$\bar{t}^1 - t^1 = -[(TAI - UTC) + (TDT - TAI)] \quad (5)$$

where $TAI-UTC$ is an integer number of leap seconds which changes approximately once a year and $TDT-TAI$ is defined to be 32.184 sec. The travel time is given by

$$t^1 - t^2 = \frac{r_{12}}{c} + 2 \frac{GM_{Earth}}{c^3} \ln \frac{r_1 + r_2 + r_{12}}{r_1 + r_2 - r_{12}} \quad (6)$$

where r_1, r_2, r_{12} are the position of the phase center of the receiver, transmitter and their difference, respectively, in an earth-centered inertial frame; t^2 in Eq. (6) is solved for iteratively given knowledge of the transmitter's orbit. For a transmitter or a receiver in space, the proper and coordinate times are related by

$$\frac{d\bar{t}^2}{dt} = \frac{GM_{Earth}}{c^2 r_2} - \frac{\dot{r}_2^2}{2c^2} + const \quad (7)$$

where the constant chosen such that proper and coordinate times agree on the surface of the earth at the equator. Eq. (7) is integrated by standard techniques to give the difference between proper and coordinate times [Wu *et al.*, 1990a].

(2) Given the estimates of $(\bar{t}^1 - t^1), (t^1 - t^2), (t^2 - \bar{t}^2)$ from the previous step, we solve for the drift of clock (2), $(\bar{t}^2 - \hat{t}^2)$, in Eq. (4.a) relative to clock (1). Similarly, we solve for $\bar{t}^3 - \hat{t}^3$ in Eq. (4.b).

(3) Assuming that clocks (2) and (3) are smooth between samples, we interpolate the corrections obtained in the previous step over the differential light time, therefore we can solve for $\bar{t}^2 - \hat{t}^2$ and $\bar{t}^3 - \hat{t}^3$.

(4) We solve for $\hat{t}^4 - \bar{t}^4$ in Eq. (4.d).

(5) We solve for $t^4 - t^2$ in Eq. (4.c) which is the desired term and corresponds to the first two terms on the right side of Eq. (3.a).

Note that in steps (2)-(5) all clock solutions are relative to clock (1), which makes the final solution of step (5) independent of that clock. The only requirement is that clocks be smooth enough between samples for proper interpolation. Based on the Selective Availability (SA)³ spectrum, a one second sampling from ground is adequate for GPS clock interpolation.

These steps are performed with GIPSY/OASIS, the software developed at JPL for precise positioning and orbit determination applications using GPS. An example of the atmospheric delay (i.e., δ_k^y in Eq. (3.b)) is illustrated in Figure 2 for an occultation obtained from the GPS/MET experiment. The occultation tangent point are located near 16°S and 171°E geodetic latitude and longitude, respectively. The leveling of the delay at the beginning of the occultation is an indication of where the ionospheric delay is dominant. The atmospheric delay of ~2.4km near the surface is larger than average; as the water vapor retrieval will later show, this can be attributed to a large moisture concentration.

Another, more straightforward but less accurate, technique (know as "double differencing") is to form the linear combination:

$$L^{24} - L^{34} - (L^{21} - L^{31}) \quad (8)$$

³ SA is the dithering of the GPS clock by the Department of Defense in order to reduce the accuracy for non-authorized users.

which causes a number of terms in Eqs. (4) to cancel out. However, only if we ignore clock drifts over the differential light time would all the clock error terms cancel out completely. For a receiver in LEO, the differential light time ranges between 0.01-0.03 seconds. A typical GPS clock error which results from SA is of ~ 6 cm/sec [Wu *et al.*, 1990b]. Therefore, ignoring the differential light time will introduce an error of 0.5-2 mm of phase measurement. The time variation of this error, which is the relevant number for occultation measurements, depends on the actual spectrum of SA. Figure 3 shows an example of this error as a function of time for about the duration of one occultation. Even though this error is small (0.1-0.3 mm/sec in general), it is not insignificant for retrievals at high altitudes.

3.2 Detecting and Fixing Breaks

In the lower troposphere several effects cause signal tracking to be difficult. These effects include the following: (1) the attenuation of the signal due to defocusing (as discussed later in section 4 and shown in shown in Fig. 5.a). (2) The significant acceleration of the atmospheric phase delay (as shown in figure 2). (3) The scintillation of the signal's amplitude and phase due to diffraction and multipath propagation caused by sharp vertical refractivity gradients. While the first two effects can be easily compensated for by having adequate receiver's antenna gain and proper tracking strategies, the third effect can be challenging and requires careful examination of the signal's power spectrum to identify the different tones corresponding to different modes of propagation. The examination of the signal's spectrum will take us outside the scope of this paper. Here, it suffices to say that the GPS receiver used for the GPS/MET experiment was not optimized to handle the complicated dynamics of the signal at the lower troposphere and it only tracked, when possible, the total sum of the multiple signals received at the LEO. During some occultations the effects mentioned above caused the receiver (which tracked at 50 Hz) to (a) slip an integer number of half-cycles at certain time updates, as shown in Figure 4.a, (b) slip a half-cycle at each time update for a certain number of consecutive time updates causing a Doppler shift bias, as shown in Figure 4.b, or (c) loose lock completely.

Figures 4.a and 4.b show examples of these effects. In order to detect half-cycle slips, which are about 10 cm, in delays that are of order 1 km, we examine the unsmoothed Doppler shift obtain by differentiating consecutive phase measurements divided by the time between measurements, Δt (e.g., 0.02 sec for GPS/MET). In this procedure a half-cycle corresponds to $1/(2 \Delta t)$ Hz (or 25 Hz for GPS/MET). Figure 4.a shows an example of the atmospheric Doppler shift obtained in this manner and detrended by subtracting a second order polynomial fit. In that example we observe two half-cycle slips at 71 and 77 sec.

Additional information on the quality of the data is obtained from the voltage signal-to-noise ratio for each measurement as recorded by the receiver. By definition, the phase thermal noise of a measurement with voltage signal-to-noise ratio of SNR_v is given by $\lambda/(2\pi SNR_v)$, where λ is the operating wavelength. Assuming thermal noise to be independent between measurements, the noise on the Doppler shift computed in the manner described above is the root-square-sum of the noise of the two phase measurements used for each point. The error bars indicated in Figure 4.a are obtained in this manner and they help identify when the deviation from the mean Doppler is due to effects other than thermal noise.

Other possible type of biases in the Doppler shift can be seen in Figure 4.b, where, starting at ~ 68 sec past the beginning of the occultation, the Doppler shift is biased by +25 Hz relative to the time before 68 sec. This is due to a half-cycle slip at each measurement

after 68 sec. In the example of Figure 4.b, the low voltage signal-to-noise ratio after 73 sec indicates that the receiver is no longer in lock.

Proper examination of the Doppler shift and the signal-to-noise ratio allows us to detect cycle slips and correct for them. For instance, the two outliers of Figure 4.a can be corrected by adding (for the first one) and subtracting (for the second one) 25 Hz. If no care is paid to detect biases and outliers in the estimated Doppler shift, these can result in biases in refractivity, which in turn creates biases in temperature, pressure or water vapor.

4. INVERSION PROCESS

4.1 Deriving Atmospheric Doppler

The result of the calibration process is to extract the sum of the neutral atmospheric and ionospheric delays for both the L1 and L2 occulted links. The atmospheric delay is normally obtained at a high rate (50 Hz for the GPS/MET experiment) for the purpose of extracting multipath signals in the lower troposphere, or for sampling the diffraction pattern induced by the atmosphere for high resolution retrievals. Our approach, however, is the Abel inversion technique which assumes geometric optics. Therefore, in order to be consistent with this assumption, we smooth the high rate data over a period corresponding to the time it takes each signal to cross a Fresnel diameter. The Fresnel diameter of the occulted signal is determined based on L1 and L2 amplitude measurements via the following set of relations:

$$F_0 = \sqrt{\frac{\lambda D_t D_r}{D_t + D_r}} \quad (9.a)$$

$$M = \left[1 + \frac{\alpha}{H} \frac{D_t D_r}{D_t + D_r} \right]^{-1} \quad (9.b)$$

$$M = \frac{I}{I_0} = \left(\frac{SNR_v}{SNR_v^0} \right)^2 \quad (9.c)$$

$$F = F_0 \sqrt{M} \quad (9.d)$$

$$V = V_0 M \quad (9.e)$$

$$T = \frac{2F}{V} = \frac{2F_0}{V_0 \sqrt{M}} \quad (9.f)$$

with

F_0, F the first Fresnel zone radius in free space and in Earth atmosphere, respectively

λ radio link wavelength

D_t, D_r distance from tangent point to transmitter and receiver respectively

M atmospheric scale factor

α bending due to Earth atmosphere

H approximate scale height of atmospheric density

I_0, I the signal intensity in free space and in Earth atmosphere

SNR_v^0, SNR_v the instrumental voltage signal-to-noise ratio recorded by the receiver in free space and in Earth atmosphere respectively

V_0, V vertical velocity of the raypath tangent point in free space and in Earth atmosphere, respectively

T time to cross a Fresnel diameter in the presence of Earth media

Knowledge of the satellites' ephemerides allows us to determine F_0 (by use of Eq. (9.a)) and V_0 . On the other hand, during an occultation, SNR_v is recorded as a function of time,

while SNR_v^0 correspond to the SNR_v at the beginning of an occultation. Based on a smoothed version of SNR_v , we compute M according to Eq. (9.c) from which we can compute F , V and T via Eqs. (9.d-9.f). The high-rate L1 and L2 phase points are then smoothed over a time interval T with a second-order polynomial fit, and the Doppler shift is derived by taking the time derivative of the fit at the middle of that interval. This smoothing guarantees that diffraction patterns caused by sub-Fresnel atmospheric structure do not appear in the retrieval. The running average is done with a time step which is usually smaller than the averaging time. This procedure is performed for each frequency independently.

For the occultation corresponding to Figure 2, Figure 5 shows the raw and smoothed L1 SNR_v , the corresponding intensity, Fresnel diameter (which roughly corresponds to the vertical resolution of the measurement), the velocity of the tangent point, and the time it takes the signal to cross a Fresnel diameter. The high concentration of water vapor causes the Fresnel diameter to decrease (~100 m), the ray tangent point to slow down (the minimum tangent point velocity in Figure 5.b is 10 m/sec) at the lowest part of the atmosphere before the signal disappears. The corresponding Doppler shift for this occultation is shown in Figure 5.c.

In order to associate a formal error to the derived Doppler, we consider the following: When averaging over N number of phase measurements, the noise in deriving the slope (which correspond to a Doppler shift) for a linear or second order fit of the phase is given by (see e.g., *Bevington*, 1969, page 115)

$$\sigma_{Doppler}^2 = \frac{N\sigma_\phi^2}{N\sum t_i^2} \quad (10)$$

where σ_ϕ^2 is the noise variance of a phase measurement (assumed to be uncorrelated in time) and t_i is the time of measurement i (for each fit the reference time is taken to the middle of the interval). Concentrating on random phase error caused by thermal noise in the receiver, σ_ϕ is given by $\lambda/2\pi SNR_v$, where λ is the operating wavelength. For large N , with Δ the time between data points (e.g., 20 msec. for GPS/MET), we can approximate the sum in the denominator of Eq. (10) by $\Delta^2 N^3/12$ and the error associated with the Doppler estimate is then given by

$$\sigma_{Doppler} = \frac{a\sigma_\phi}{\Delta N^{3/2}} \quad (11)$$

where $a = \sqrt{12}$. (The general form of Eq. (11) is valid for polynomial fit to the data of any order but the value of a changes with the order of the polynomial fit; e.g., $a = 76$ for a third order polynomial.)

We take advantage of this rapid decrease in the Doppler noise with N in order to minimize the estimated atmospheric Doppler at high latitudes where the atmosphere is tenuous. For instance, if we desire to reach a specific accuracy $\sigma_{Desired}$, then we need to average over N points, where N is given by

$$N \approx \left(\frac{a\sigma_\phi}{\Delta\sigma_{Desired}} \right)^{2/3} \quad (12)$$

In practice, when deciding on the appropriate number of phase measurement points to average, we choose the maximum of N (of Eq. (12)) or T/Δ (where T is given by Eq. (9.f)).

4.2 Deriving Atmospheric Bending

The atmospheric Doppler shift can be used to derive the atmospheric bending, α , as a function of the asymptotic miss distance, a (Figure 1). The atmospheric Doppler shift, Δf , can be related to the direction of the transmitted and received signals by the expression

$$\frac{d\delta}{dt} = \lambda\Delta f = [\mathbf{v}_t \cdot \hat{\mathbf{k}}_t - \mathbf{v}_r \cdot \hat{\mathbf{k}}_r - (\mathbf{v}_t - \mathbf{v}_r) \cdot \hat{\mathbf{k}}] \quad (13)$$

with:

\mathbf{v}_t and \mathbf{v}_r the transmitter and receiver's velocity respectively,

$\hat{\mathbf{k}}_t$, $\hat{\mathbf{k}}_r$ the unit vectors in the direction of the transmitted and received signal respectively (Figure 6)

$\hat{\mathbf{k}}$ the unit vector in the direction from the transmitter to the receiver.

Eq. (13) is derived by differencing the Doppler shift observed in the presence of the atmosphere and the Doppler shift that would be observed for the same transmitter-receiver geometry in the absence of the atmosphere. The first-order relativistic contributions to the Doppler are identical in the two situations and cancel out.

Note that this equality is true in general regardless of the shape of the atmosphere; however, Eq. (13) has an infinite number of solutions since $\hat{\mathbf{k}}_t$ and $\hat{\mathbf{k}}_r$ are both unknown, corresponding to four independent parameters. Therefore, certain assumptions have to be made on the shape of the atmosphere in order to derive the atmospheric bending from Eq. (13).

To a very good approximation, the neutral atmosphere is spherically symmetric. In order to account for the ellipticity of the Earth, the center of symmetry is taken to correspond to the circle in the occultation plane which best fits the geoid near the tangent point. Since an occultation may not take place entirely in one plane, the center of symmetry is based on the plane determined by the lowest link of the occultation. This center is then fixed for the entire occultation, and can be as far as 40 km from the real center of the Earth. Once a center of symmetry is defined, all variables (such as α and a) are defined with respect to that center.

With the spherical symmetry assumption, Eq. (13) reduces to the equation in two unknowns

$$\frac{d\delta}{dt} = (v_t \cos(\phi_t - \delta_t) - v_r \cos(\phi_r - \delta_r)) - (v_t \cos \phi_t - v_r \cos \phi_r) \quad (14.a)$$

(the angles are defined in Figure 6). In addition, the *formula of Bouguer* (equivalent to Snell's law in a spherically symmetric medium) states that [e.g., *Born and Wolf*, 1980, page 123]

$$a = r_t n_t \sin(\theta_t + \delta_t) = r_r n_r \sin(\theta_r + \delta_r) \quad (14.b)$$

with:

$\mathbf{r}_t, \mathbf{r}_r$ the vectors from the center of curvature to transmitter and receiver, respectively

$r_t = |r_t|$ and $r_r = |r_r|$
 n_t and n_r , the indices of refraction at the transmitter and receiver, respectively.

At the heights of the transmitter (~20000km) and receiver (low-Earth orbit), the indices of refraction are assumed equal to 1. This approximation can be shown to introduce a very small error in the estimated bending in the ionosphere [Hajj and Romans, 1998], and it cancels completely after doing the ionospheric calibration to estimate the neutral atmospheric bending. The angles δ_t and δ_r are determined by simultaneously solving Eqs. (14.a) and (14.b) (easily accomplished using Newton's method and a first guess of $\delta_t = 0$ and $\delta_r = 0$). The total bending is $\alpha = \delta_t + \delta_r$, and the corresponding a is obtained from Eq. (14.b). Figure 7 shows an example of the bending derived for L1 and L2. The error assigned to the bending is obtained via the simple scaling

$$\sigma_\alpha = \frac{\sigma_{Doppler}}{V_0} \quad (15)$$

where V_0 is the same as in Eq. (9.e) and σ_α is given in units of radians.

4.3 Ionospheric Calibration

Because of the dispersive nature of the ionosphere, the L1 and L2 links travel along slightly different paths and have slightly different bending (as depicted in Figure 1). The separation of the two signals at ionospheric heights near the tangent point varies between less than a hundred meters to 5 km, depending on the tangent height of the occulted signal, the solar conditions, local time and the location of the occultation. (For this effect and other ionospheric effects on GPS occultations see, e.g., Hajj and Romans, 1998.) In the most general situation, an ionospheric correction is needed in order to estimate the neutral atmospheric bending. In our approach we follow a procedure first suggested by Vorob'ev and Krasil'nikova [1994]. Let $\alpha_1(a_1)$ and $\alpha_2(a_2)$ be the bending as a function of the asymptote miss distance for the L1 and L2 signals, respectively. The linear combination

$$\alpha_{neut}(a_o) = \frac{f_1^2}{(f_1^2 - f_2^2)} \alpha_1(a_o) - \frac{f_2^2}{(f_1^2 - f_2^2)} \alpha_2(a_o) \quad (16)$$

where α_1 and α_2 are interpolated to the same value of a_o , removes the first order ionospheric bending (which is proportional to f^2). The two coefficients on the right side of Eq. (16) have the numerical values to 2.5457.. and 1.5457.., respectively.

The interpolation scheme we use is piecewise cubic, within each interval $t_i < t < t_{i+1}$ between data points. The interpolating cubic polynomial $f(t)$ is determined by four conditions fixing the fit and its derivative at the endpoints, in terms of the four data values $f_{i-1}, f_i, f_{i+1}, f_{i+2}$. Specifically, the conditions are: $f(t_j) = f_j$ and $f'(t_j) = (f_{j+1} - f_{j-1}) / (t_{j+1} - t_{j-1})$ for $j = i, i+1$. This "smooth-cubic" interpolation scheme avoids introducing sharp variations between the points when the data is noisy (in contrast to traditional cubic splines), and is used throughout the remainder of the inversion process (including the Abel transform and the hydrostatic integrals).

Based on Eq. (16), the noise associated with the neutral atmospheric bending is given by

$$\sigma_{\alpha_{neut}}^2 = (2.54)^2 \sigma_{\alpha_1}^2 + (1.54)^2 \sigma_{\alpha_2}^2. \quad (17)$$

L2 phase measurements are usually noisier than L1 phase measurements for several reasons. First, the L2, which has a lower frequency than L1, is more influenced by ionospheric scintillation and delay. Second, the C/A code is transmitted with 3dB more power than the P1 code, which in turn is 1-3dB stronger than the P2. The relative strength of C/A relative to P1 and P2 also depends on whether or not the Department of Defense (DoD) anti-spoofing (AS) is activated, and on the type of the receiver and tracking strategy. In general, L1 phase derived based on C/A is more accurate than L2.

However, even under conditions where both L1 and L2 noise are comparable, Eq. (17) implies that the noise introduced by the ionospheric-free linear combination is about a factor of 3 larger than individual signal noise. We overcome this limitation by redefining the bending in Eq. (16) as

$$\alpha_{neut}(a_o) = 1.54\alpha_1(a_o) + (\bar{\alpha}_1(a_o) - \bar{\alpha}_2(a_o)) \quad (18)$$

where $\bar{\alpha}_1$ and $\bar{\alpha}_2$ are the L1 and L2 bending smoothed over longer intervals than discussed in section 4.2. The longer smoothing interval is normally of order 2-sec (100 points of 50 Hz data), which, relative to a Fresnel diameter smoothing (~26 points of 50 Hz data), should correspond to noise about a factor of 7 smaller, according to Eq. (11).

The calibration should not be continued above a certain height, when the neutral atmosphere signature on the occulted signal is comparable to residual ionospheric effects or the receiver's thermal noise. This height is determined by computing a moving χ^2 based on departures from an exponential fit to ionospheric-free bending, and discontinuing the calibration after χ^2 exceeds a specified value. This tends to occur at a height of order ~50-90 km, depending on the ionospheric conditions.

Deeper in the atmosphere, due to defocusing effects and the weakening of the signal, the L2 signal is not used when the SNR_v drops below a certain limit. An extrapolation of the ionospheric correction is used from higher altitudes to correct for the ionosphere. The ionospheric-free bending for our example occultation is shown in Figure 7.

For ionospheric retrievals, the bending from one frequency is used above 60 km.

4.4 The Abel Inversion

In a spherically symmetric atmosphere, from the formula of Bouguer [*Born and Wolf*, 1980, p. 123], the signal's bending can be related to the index of refraction via the integral

$$\alpha(a) = -2a \int_a^\infty \frac{1}{\sqrt{a'^2 - a^2}} \frac{d \ln(n)}{da'} da', \quad (19)$$

This integral equation can then be inverted by using an Abel integral transform given by [see, e.g., *Tricomi*, 1985, p. 39]

$$\ln(n(a)) = \frac{1}{\pi} \int_a^\infty \frac{\alpha(a')}{\sqrt{a'^2 - a^2}} da'. \quad (20)$$

the upper limit of the integral in (13) requires knowledge of the bending as a function of a up to the top of the atmosphere. In practice, however, the estimated bending is reasonably accurate only up to a certain upper height, a_u , as described in 4.3. Therefore, we use a least-square estimator of α based on measured bending, α_m , and estimated bending (from an *a priori* model), α_e , weighted by their corresponding uncertainties, σ_m and σ_e ; therefore,

$$\alpha(a) = A(a) \left(\frac{\alpha_m(a)}{\sigma_m^2(a)} + \frac{\alpha_e(a)}{\sigma_e^2(a)} \right); \quad A(a) = \left(\frac{1}{\sigma_m^2(a)} + \frac{1}{\sigma_e^2(a)} \right)^{-1}. \quad (21)$$

In order to make the occultation retrieval completely independent of the model below a certain height, a_u (50 km, in our example), σ_e is effectively set to infinity below this height. Therefore, after substituting (21) in (20), we obtain

$$\ln(n(a)) = \frac{1}{\pi} \int_a^{a_u} \frac{\alpha_m(a')}{\sqrt{a'^2 - a^2}} da' + \frac{1}{\pi} \int_{a_u}^{\infty} \frac{A(a')}{\sigma_m^2(a')} \frac{\alpha_m(a')}{\sqrt{a'^2 - a^2}} da' + \frac{1}{\pi} \int_{a_u}^{\infty} \frac{A(a')}{\sigma_e^2(a')} \frac{\alpha_e(a')}{\sqrt{a'^2 - a^2}} da'. \quad (22)$$

Furthermore, in order to avoid numerically integrating over a weak singularity at the lower boundary of the first integral on the right side of (22), we rewrite it as

$$\begin{aligned} \int_a^{a_u} \frac{\alpha_m(a')}{\sqrt{a'^2 - a^2}} da' &= \left[\alpha(a_{\text{int}}) \ln \left(a_{\text{int}} + \sqrt{a_{\text{int}}^2 - a^2} \right) \right. \\ &\quad \left. - \alpha(a) \ln(a) - \int_a^{a_{\text{int}}} \ln \left(a'^2 + \sqrt{a'^2 - a^2} \right) \frac{d\alpha(a')}{da'} da' \right] \\ &\quad + \int_{a_{\text{int}}}^{a_u} \frac{\alpha_m(a')}{\sqrt{a'^2 - a^2}} da' \end{aligned} \quad (23)$$

where a_{int} is an intermediate value between a and a_u and is normally chosen to be slightly larger than a . The terms in brackets on the right-hand side of (23) are the result of integration by parts. Eq. (22) yield the index of refraction, n , as a function of a , at the tangent point (TP). The TP radius is obtained from $r = a/n$. The radius in turn is converted into height above an ellipsoidal fit to the mean sea-level geoid. Figure 8.a shows the retrieved refractivity as a function of height for our occultation example.

We can convert the independent coordinate from height to geopotential height. First we convert all of the tangent point locations into displacements from the center of the Earth. We compute the sum of the gravitational and centrifugal potential energies per unit mass at each position. The gravitational potential energy per unit mass is computed using a version of the JGM-3 gravity model [Tapley *et al.* 1996]. This version is a 64-th degree spherical harmonic expansion which can reproduce the mean sea-level geoid with an accuracy of tens of centimeters. The potential of the mean sea-level geoid is subtracted from the sum of the gravitational and centrifugal potentials, and the difference is then divided by a standard value of gravitational acceleration to give the geopotential height. The geopotential height can then substitute for height as the independent coordinate for all derived profiles [Leroy, 1997].

For ionospheric retrievals, the retrieval is performed from 60 km up to the height of the LEO satellite. Above the LEO satellite, the bending is extrapolated with an exponential fit [Hajj and Romans, 1998].

4.5 Deriving Geophysical Parameters From Refractivity

The refractivity, N , is related to geophysical quantities via

$$N = (n - 1) \times 10^6 = a_1 \frac{P}{T} + a_2 \frac{P_w}{T^2} - 40.3 \times 10^6 \frac{n_e}{f^2} + O\left(\frac{1}{f^3}\right) \quad (24)$$

with $a_1 = 77.6$ K/mbar

$a_2 = 3.73 \times 10^5 \text{ K}^2/\text{mbar}$
 P total pressure
 T temperature
 P_w water vapor partial pressure
 n_e electron density (m^{-3})
 f operating frequency (Hz).

When the signal is passing through the ionosphere (tangent point height $> 60 \text{ km}$), the first two terms on the right side of (24) can be ignored, as well as higher order ionospheric terms in the ionosphere. Therefore, measurement of n directly corresponds to electron density in the ionosphere.

In the neutral atmosphere (tangent point high $< 60 \text{ km}$), the ionospheric calibration process described in section 4.3 above effectively removes the first order ionospheric term ($1/f^2$) in Eq. (24). (Higher order contributions constitute the major source of error during day-time solar maximum at high altitudes; see *Kursinski et al.*, 1997, for an estimate of these errors and *Bassiri and Hajj*, 1994, for possible means of correcting them.) In order to solve for P , T , and/or P_w given N we use the additional constraints of hydrostatic equilibrium and the ideal gas law:

$$\frac{dP}{dh} = -g\rho, \quad (25)$$

$$\rho = \rho_d + \rho_w = \frac{m_d P}{TR} + \frac{(m_w - m_d) P_w}{TR}, \quad (26)$$

with

h height,

g gravitational acceleration,

ρ , ρ_d , ρ_w total, dry air and water vapor densities respectively,

m_d , m_w mean molecular mass of dry air and water vapor respectively,

R universal gas constant.

Combining Eqs. (25) and (26), and using equation (24) (ignoring the ionospheric terms) to substitute for P/T , we obtain

$$\frac{dP}{dh} = -\frac{gm_d}{a_1 R} N + \frac{a_2 gm_d}{a_1 R} \frac{P_w}{T^2} + \frac{g(m_d - m_w)}{R} \frac{P_w}{T}. \quad (27)$$

Given N , we have a system of two equations (24 and 27) and three unknowns (T , P , and P_w). Because saturation vapor pressure decreases rapidly with decreasing temperature, as dictated by the Clausius-Clapeyron equation, P_w can be ignored above the tropospheric height corresponding to $T = 250\text{K}$; therefore, given N , both T and P can be solved for in the upper troposphere and the stratosphere from equations (24) and (27) and a boundary condition (usually taken to be a temperature boundary condition at $\sim 50 \text{ km}$). The solution to P and T as a function of height for our occultation example are shown in Figure 8.a and 8.b, respectively. For comparison, T from the ECMWF nearest 6 hourly analysis and interpolated to the location of the occultation, is also shown in Figure 8.b. Both the GPS/MET and ECMWF analysis temperature agree to better than 2K everywhere except near the tropopause, where the analysis misses the double tropopause detected by the GPS/MET retrieval.

When P_w is significant, such as in the middle and lower troposphere, it is necessary to have an independent knowledge of one of the three parameters (T , P , P_w) in order to solve for the other two. Given that temperature is generally better known and less variable than water vapor, it is more efficient to assume knowledge of T , and then solve for P and P_w .

The exact relation between errors in T , P and P_w is a function of latitude and height and is described in detail by *Kursinski et al.* [1995].

Assuming knowledge of $T(h)$ and pressure at some height for a boundary condition, then equations (24) and (27) are solved iteratively as follow:

- (1) Assume $P_w(h) = 0$ for a first guess
- (2) Integrate equation (27) to obtain $P(h)$
- (3) Use $P(h)$ and $T(h)$ in (24) to update $P_w(h)$
- (4) repeat steps (2) and (3) until convergence.

Given P and P_w , specific humidity, q , (defined as the ratio of water vapor density to the moist air density), is given by

$$q = \left[\frac{m_d}{m_w} \left(\frac{P}{P_w} - 1 \right) + 1 \right]^{-1} \approx \frac{m_w}{m_d} \frac{P_w}{P}. \quad (28)$$

The solution of specific humidity for our example, using T from the ECMWF analysis, is shown in Figure 8.c. For comparisons, specific humidity from the ECMWF analysis is also shown on Figure 8.c. The retrieved specific humidity at the surface is close to the maximum that is normally observed on Earth. This explains why the delay and bending observations are quite larger than average near the surface.

It is notable that in the occultation example shown the signal was tracked virtually down to the surface, in spite the very large humidity there. The time during which this occultation was taken (June 23, 1995 which is during the second prime GPS/MET period), corresponded to a time where a special tracking software was operating which had improved the tracking in the lower troposphere substantially over the other two prime time periods (for more detail on this see discussion by *Kursinski and Hajj*, 1999).

5. EXAMPLES OF GPS/MET RETRIEVALS AND COMPARISONS TO ECMWF

Here we briefly present other examples of GPS/MET profiles obtained with the system described above, and compare them to corresponding profiles obtained from the nearest 6-hour ECMWF analysis interpolated to the location of the occultation.

Figure 9 shows the results from four different GPS/MET occultation (the three plots aligned horizontally correspond to the same occultation). The date, time, occulting GPS satellite, latitude and longitude of the occultation is indicated at the top of each plot. For each occultation we plot the fractional difference between the GPS/MET and ECMWF refractivity (plots on left), the GPS/MET (solid line) and ECMWF (dashed line) temperatures (middle plots), the GPS/MET (solid line) and ECMWF (dashed line) water vapor pressures (plots on right). These occultations are representative of other occultations obtained during the period of June 21-July 4, 1995, and are chosen to represents different atmospheric conditions (i.e., different latitudes and moisture content).

GPS/MET and ECMWF fractional refractivity plots indicate that refractivity agree to better than 1% in dry regions. Large refractivity differences (up to 6%) appear at lower altitude and can be attributed to differences in moisture. Theoretical estimate indicates that refractivity derived from GPS occultations is accurate to about 1% near the surface and improves at higher latitude (up to ~40 km) [*Kursinski et al.*, 1997].

More T retrievals obtained from GPS/MET using the described occultation retrieval system as well as statistical comparisons to atmospheric models are discussed by *Hajj et al.*, [1995] and *Kursinski et al.*, [1996]. Also retrievals of geopotential height as a function of

pressure from GPS/MET and comparison to ECMWF analysis are discussed by Leroy [1997]. A detailed water vapor analysis from GPS/MET is given by Kursinski and Hajj, 2000.

6. SUMMARY/CONCLUSION

We described a system developed at JPL to process GPS occultation data for retrieving refractivity, temperature, pressure and geopotential height in the neutral atmosphere and ionospheric free electron density in the ionosphere. Although the concept of radio occultation is a simple one, care must be taken at different steps in the processing of the data in order to obtain accurate retrievals. The system described can be divided into two major parts. First, the calibration of the signal, which implies isolating the atmospheric delay induced on the occulted signal from all other effects such as geometrical motion of the satellites, clocks and ground troposphere. Second, the inversion of the atmospheric delay to obtain physical parameters such as refractivity and other derived products. Our system relies on the most basic approach of using the Abel inversion to obtain refractivity in the atmosphere. Several improvements over the Abel inversion are already suggested by different investigators as mentioned earlier; however, the Abel inversion will always serve as a robust approach to obtain a first order solution (and a very accurate one for the neutral atmosphere as demonstrated by several investigations cited above) to the atmospheric state.

Assimilation of occultation data into weather models has been considered by several investigators at different levels, including atmospheric phase delay as a function of time, Doppler shift as a function of time, bending angle as a function of asymptotic miss distance, and refractivity as a function of geopotential height. All of these approaches, however, would still require the first stage of processing, namely, the calibration stage and some ionospheric calibration.

Even though the scope of this work was not to demonstrate how lower tropospheric sensing can be done with GPS on a routine basis, our example demonstrates that it is at least feasible to track the GPS signal down to the surface under very humid conditions. In a future work, we will discuss how lower tropospheric sensing can be obtained at virtually all times with GPS occultation.

ACKNOWLEDGMENT:

This work was done at the Jet Propulsion Laboratory of the California Institute of Technology, with funding from the National Aeronautics and Space Agency, Integrated Program Office, and JPL's Director Research Discretionary Funds.

REFERENCES:

- Bevington, P. R., *Data Reduction and Error Analysis for the Physical Sciences*, McGraw-Hill Book Company, New York, 1969.
- Bassiri S. and G. A. Hajj, Higher-order ionospheric effects on the Global Positioning System observables and means of modeling them, *manuscripta geodaetica*, 18:280-289, 1993.
- Bevington P. R., *Data Reduction and Error Analysis for the Physical Sciences*, McGraw-Hill book company, N. Y., 1969.
- Born, M., and E. Wolf, *Principles of Optics*, 6th ed., Pergamon, Tarrytown, N. Y., 1980.
- Eyre, J. R., Assimilation of radio occultation measurements into a numerical weather prediction system. ECMWF Technical Memorandum No. 199, 1994.
- Fjeldbo, G. and V. R. Eshleman, Atmosphere of Venus as Studied with the Mariner 5 Dual Radio-Frequency Occultation Experiment. *Radio Sci.*, 4, 879-897, 1969.

- Fjeldbo, G. F., V. R. Eshleman, and A. J. Kliore, The neutral atmosphere of Venus as studied with the Mariner V radio occultation experiments, *Astron. J.*, 76, 123-140, 1971.
- Gorbunov M. E., A. S. Gurvich, L. Bengtsson, Advanced algorithms of inversion of GPS/MET Satellite data and their application to reconstruction of temperature and humidity, Max-Planck-Institute fur Meteorologie Report No. 211, F. R Germany, August 1996b.
- Gorbunov, M. E. and S. V. Sokolovskiy, Remote Sensing of refractivity from space for global observations of atmospheric parameters. Max-Planck-Institute fur Meteorologie Report No. 119, Hamburg, Germany, 1993.
- Gorbunov, M. E., S. V. Sokolovsky, and L. Bengtsson, Space refractive tomography of the atmosphere: Modeling of direct and inverse problems, Max-Planck-Inst. Fur Meteorology Report No. 210, Hamburg, F. R. Germany, August 1996a.
- Gorbunov, M. E., Three-dimensional satellite refractive tomography of the atmosphere: Numerical-simulation, *Radio Sci.*, 31, 95-104, 1996.
- Gurvich, A. S. and T. G. Krasil'nikova, Navigation satellites for radio sensing of the Earth's atmosphere, *Sov. J. Remote Sensing*, 7, 1124-1131, 1990.
- Hajj, G. A., and L. J. Romans, Ionospheric electron density profiles obtained with the Global Positioning System: Results from the GPS/MET experiment, *Radio Sci.*, 33, 175-190, 1998.
- Hajj, G. A., E. R. Kursinski, W. I. Bertiger, S. S. Leroy, T. Meehan, L. J. Romans, and J. T. Schofield, Initial results of GPS-LEO occultation measurements of Earth's atmosphere obtained with the GPS/MET experiment, Proc. IAG Symp. G1, GPS Trends in Precise Terrestrial, Airborne, and Spaceborne Applications, IUGG XXI General Assy., Boulder, CO, 2-14 July 1995, Springer-Verlag, 1996.
- Hajj, G. A., L. J. Romans, W. I. Bertiger, E. R. Kursinski and A. J. Mannucci, Imaging the ionosphere with GPS/MET, *Proc. of URSI GPS/MET Workshop*, Tucson, Arizona, Feb. 21-23, 1996.
- Hajj, G. A., R. Ibanez-Meier, E. R. Kursinski, and L. J. Romans, Imaging the ionosphere with the Global Positioning System, *Int. J. Imaging Syst. Technol.*, 5, 174-184, 1994.
- Hoeg, P., A. Hauchecorne, G. Kirchengast, S. Syndergaard, B. Belloul, R. Leitinger, W. Rothleitner, Derivation of atmospheric properties using radio occultation technique, Scientific Report 95-4, Danish Meteorological Institute, Copenhagen, Denmark, 1995.
- Kuo Y.-H., X. Zou, W. Huang, The impact of global positioning system data on the prediction of an extratropical cyclone-An observing system simulation experiment, *J. Dyn. Atmos. Ocean*, 27, 439-470, 1998.
- Kursinski, E. R., G. A. Hajj, et al., Initial results of radio occultation observations of Earth's atmosphere using the Global Positioning System, *Science*, 271, 1107-1110, 1996.
- Kursinski, E. R. and G. A. Hajj, An examination of water vapor derived from GPS occultation observations during June-July 1995, submitted to *J. Geophys. Res.*, 2000.
- Kursinski, E. R., G. A. Hajj, K. R. Hardy, J. T. Schofield, and R. Linfield, Observing Earth's atmosphere with radio occultation measurements, *J. of Geophys. Res.*, 102(D19), 23429-23465, 1997.
- Kursinski, E. R., G. A. Hajj, K. R. Hardy, L. J. Romans and J. T. Schofield, Observing tropospheric water vapor by radio occultation using the Global Positioning System, *Geophys. Res. Lett.*, 22, 2365-2368, 1995.
- Leitinger, R., H.-P. Ladreiter, and G. Kirchengast, Ionosphere tomography with data from satellite reception of Global Navigation Satellite System signals and ground reception of Navy Nav Satellite System signals, *Radio Sci.*, 32(4), 1657-1669, 1997.
- Leroy, S. S., Measurement of geopotential heights by GPS radio occultation, *J. Geophys. Res.*, 102, 6971-6986, 1997.
- Lindal, G. F., J. R. Lyons, D. N. Sweetnam, V. R. Eshleman, D. P. Hinson, and G. L. Tyler, The atmosphere of Neptune: Results of radio occultation measurements with the Voyager 2 spacecraft. *Geophys. Res. Lett.*, 17, 1733-1736, 1990.

- Lindal, G. F., The Atmosphere of Neptune: An Analysis of Radio Occultation Data Acquired with Voyager, *Astronomical J.*, 103, 967-982, 1992.
- Melbourne, W. G., E. S. Davis, C. B. Duncan, G. A. Hajj, K. R. Hardy, E. R. Kursinski, T. K. Meehan, L. E. Young, and T. P. Yunck, The application of spaceborne GPS to atmospheric limb sounding and global change monitoring, JPL Publ. 94-18, Pasadena, California, April 1994.
- Rius, A., G. Ruffini, A. Romeo, Analysis of ionospheric electron-density distribution from GPS/MET occultations, *IEEE Trans. on Geoscience and Remote Sensing*, 36(2), 383-394, 1998.
- Schreiner W. S., S. S. Sokolovskiy, C. Rothen, R. H. Ware, Analysis and validation of GPS/MET radio occultation data in the ionosphere, *Radio Sci.* 34(4) 949-966, 1999.
- Sovers O. J. and J. S. Border, Observation model and parameter partials for the JPL geodetic GPS modeling software "GPSOMC", JPL Publication 87-21, Rev. 2, June, 1990.
- Spilker, J. J., GPS signal structure and performance characteristics, *Global Positioning System*, Institute of Navigation, Washington, D.C., pp. 29-54, 1980.
- Steiner, A. K., G. Kirchengast, H. P. Ladreiter, Inversion, error analysis, and validation of GPS/MET occultation data, *Ann. Geophysicae* 17, 122-138, 1999.
- Tapley, B. D., M.M. Watkins, J.C. Ries, G.W. Davis, W.J. Eanes, S.R. Poole, H.J. Rim, B.E. Schutz, and C.K. Shum. The JGM-3 gravity model. *J. Geophys. Res.*, 101, 28029-28049, 1996.
- Tyler, G. L., Radio propagation experiments in the outer solar system with Voyager, *Proc. IEEE*, 75, 1404-1431, 1987.
- Vorob'ev, V. V., and T. G. Krasil'nikova, Estimation of the accuracy of the atmospheric refractive index recovery from Doppler shift measurements at frequencies used in the NAVSTAR system, *Phys. Atmos. Ocean*, 29, 602-609, 1994.
- Ware, R., et al., GPS sounding of the atmosphere from low earth orbit: Preliminary results, *Bull. Am. Meteorol. Soc.*, 77(1), 19-40, 1996.
- Wu J. T., S. C. Wu, G. A. Hajj, W. I. Bertiger and S. M. Lichten, Effects of antenna orientation on GPS carrier phase, *manuscripta geodaetica*, 18, 91-98, 1993.
- Wu S. C., W. I. Bertiger, and J. T. Wu, Minimizing selective availability error on TOPEX GPS measurements, paper presented at the Conference on Astrodynamics, Am. Inst. of Aeronaut. and Astronaut./Am. Astron. Soc., Portland, Oreg., Aug. 20-22, 1990b.
- Wu S. C., Y. Bar-Sever, S. Bassiri, W. I. Bertiger, G. A. Hajj, S. M. Lichten, R. P. Malla, B. K. Trinkle, J. T. Wu, Global positioning system precision orbit determination software design, JPL Publication D-7275, March, 1990a.
- Yuan, L. L., R. A. Anthes, R. H. Ware, C. Rocken, W. D. Bonner, M. G. Bevis and S. Businger, Sensing climate change using the global positioning system, *J. Geophys. Res.*, 98, 14,925-14,937, 1993.
- Yunck, T. P., G. F. Lindal, and C. H. Liu, The role of GPS in precise earth observation, paper presented at the IEEE Position, Location and Navigation Symposium, Orlando, Fl., Nov. 29-Dec. 2, 1988.
- Zou X., Y.-H. Kuo and Y. R. Guo, Assimilation of atmospheric radio refractivity using a nonhydrostatic adjoint model. *Mon. Wea. Rev.*, 123(7), 2,229-2,249, 1995.

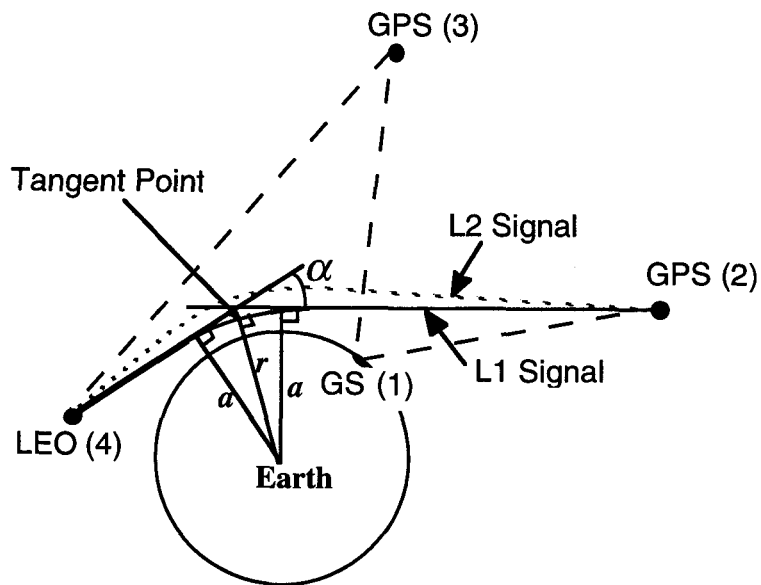


Figure 1: GPS occultation geometry defining the tangent point, the asymptote miss distance, a , and depicting how the L1 and L2 signals travel slightly different paths due to the dispersive ionosphere. Also shown are the other non-occluding GPS transmitter and ground receiver used for calibration.

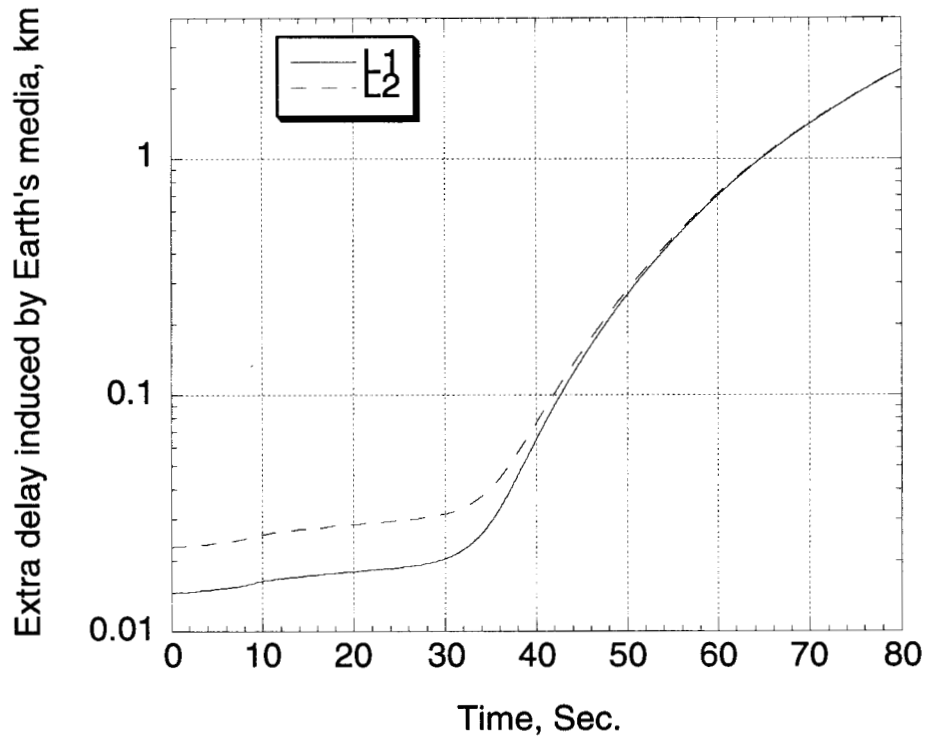


Figure 2: Extra phase delay induced by the ionosphere and the neutral atmosphere on an occulted signal at 50Hz rate. The occultation event is between GPS/MET and GPS satellite No. 31. Time 0 corresponds to 1995-6-23:0156.30 UT. The flattening of the curves at the beginning of the occultation is due to the dominant ionospheric delay at these heights.

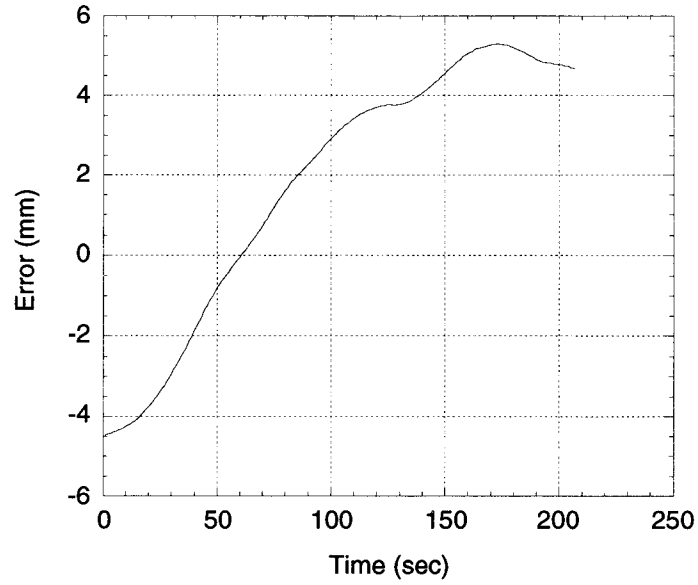


Figure 3: The error introduced by straight double differencing over the span of an occultation. This is estimated by assuming a differential travel light time of 0.01 seconds and based on the behavior of the GPS clocks with SA on. This error is eliminated by properly solving for the clocks accounting for the travel light time.

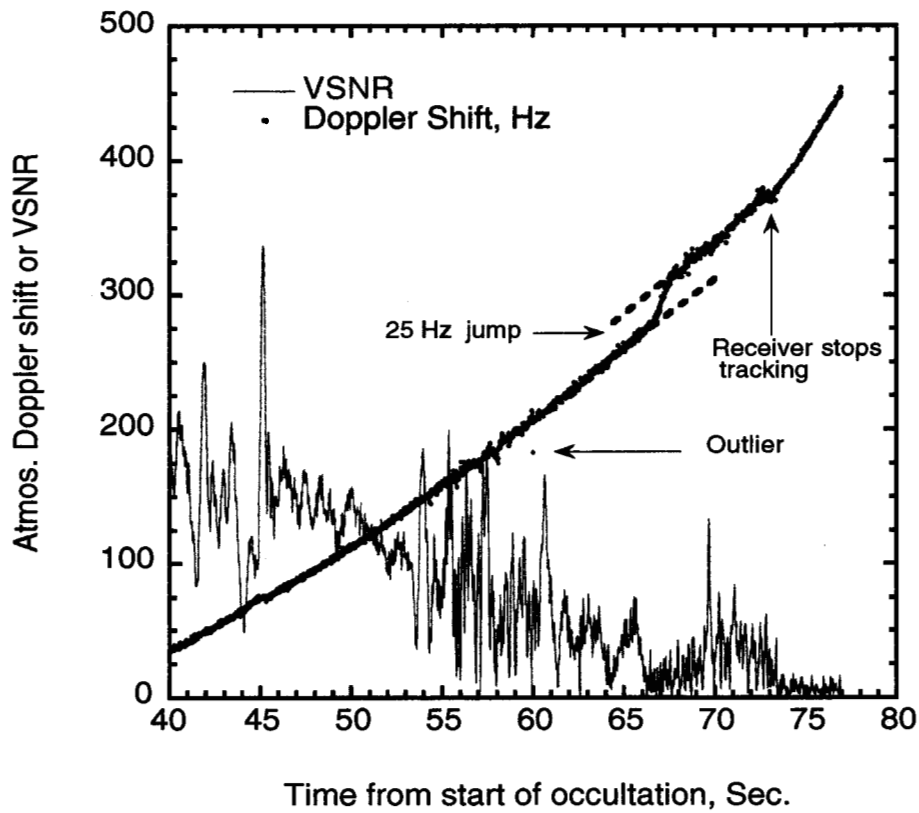
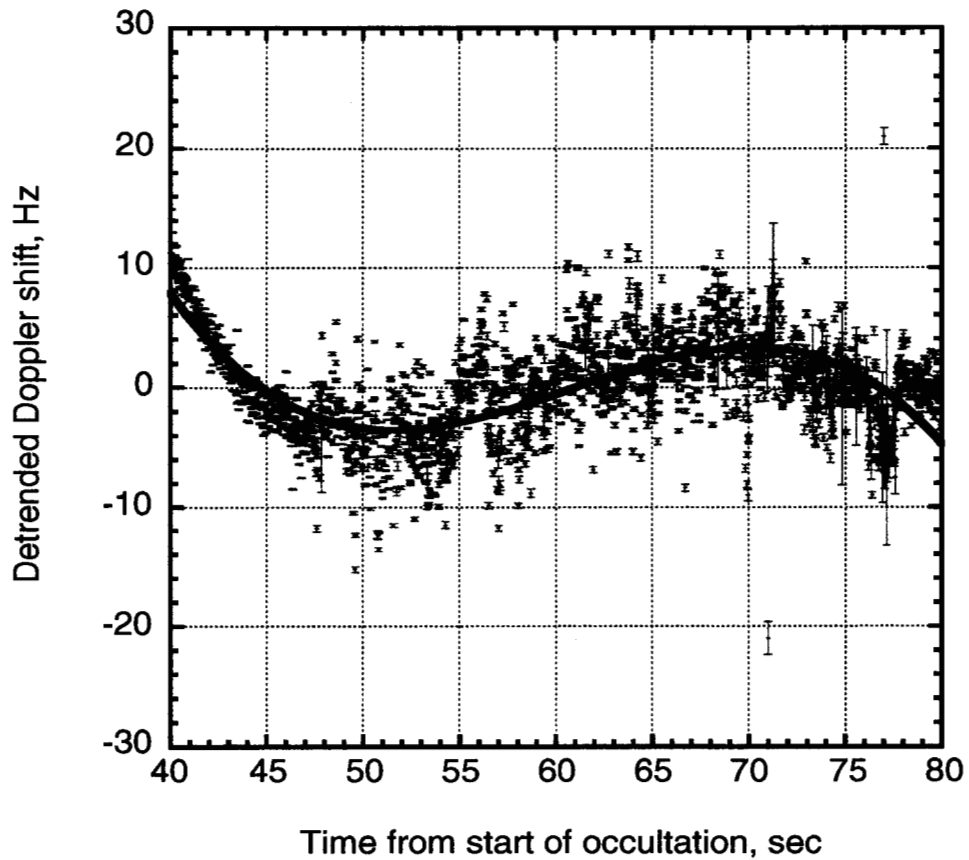


Figure 4: (Top-a) The atmospheric Doppler shift on the occulted signal corresponding to the occultation of figure 2 after subtracting a second order polynomial fit. The figure shows two outliers at ~71 and ~77 sec. which correspond to half-cycle slips in the receiver. The error bars are estimated from the signal-to-noise ratio information recorded in the receiver. The solid line is a third order polynomial fit to the data. (Bottom-b) The atmospheric Doppler shift on the occulted signal corresponding to an occultation between GPS/MET-GPS23 starting at 1995-06-23-0031.20 UT. Close examination of the Doppler shift shows: (1) one half-cycle slip at ~60 sec, (2) a half-cycle slip at each of the 50 Hz point after ~68 sec resulting in the Doppler shift bias of +25 Hz, (3) a change in the slope of the Doppler shift at about 73 sec, where the voltage signal-to-noise ratio indicates that the receiver is out-of-lock beyond that point.

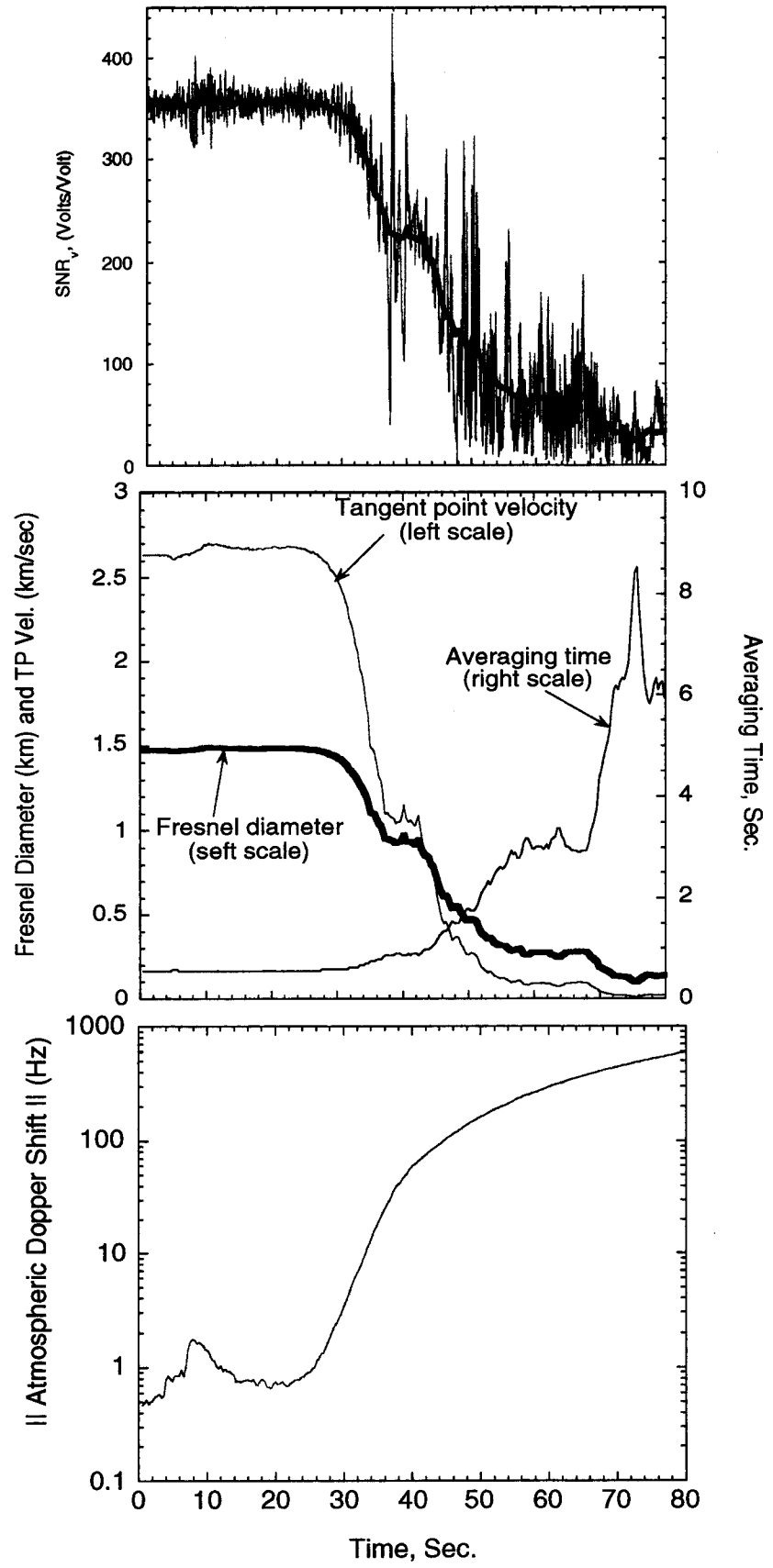


Figure 5: (Top–a) High rate (thin line) and smoothed (thick line) L1 voltage signal-to-noise ratio for the same occultation event as in Figure 2. (Middle–b) The Corresponding Fresnel diameter (which sets roughly the vertical resolution), the vertical velocity of the tangent point and the corresponding averaging time of the signal, derived based on Eqs. (9.a-f). A running time average with time steps of 0.33 sec is used to derive the Doppler shift and bending. (Bottom–c) The absolute value of atmospheric Doppler shift of the occultation. For descending occultations, the atmospheric delay increases with time causing the signal to be blue shifted, therefore the atmosphere introduces a negative Doppler shift. The reverse is true of ascending occultations.

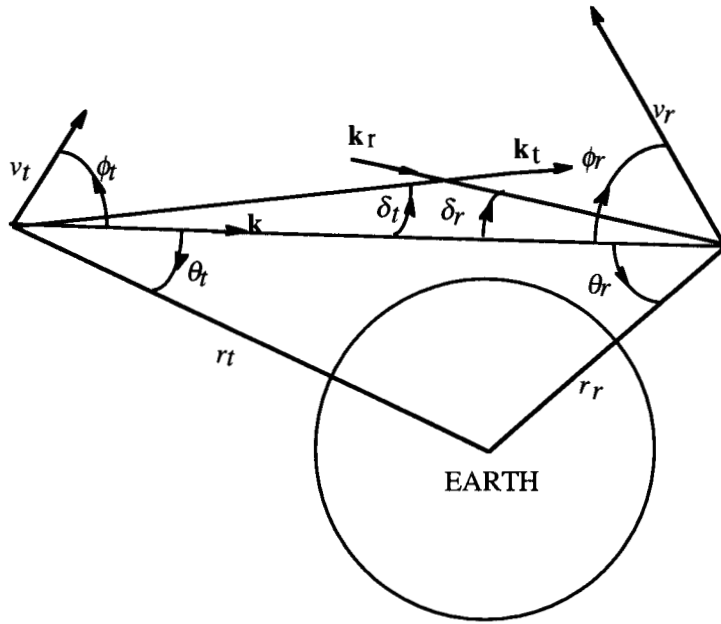


Figure 6: Occultation geometry defining the angles used in Eqs. (14.a-b).

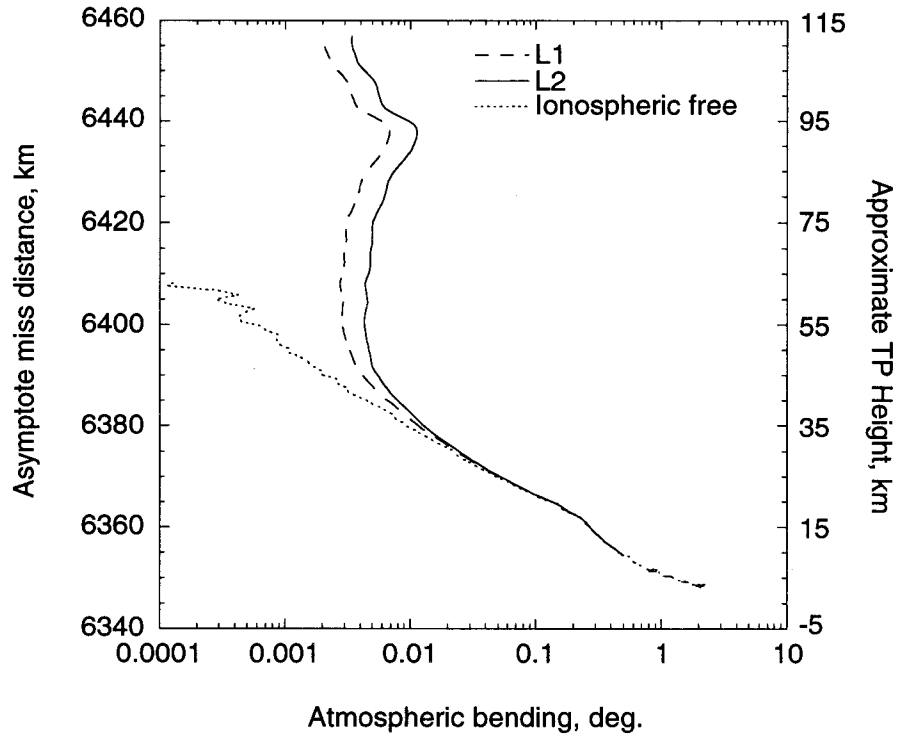
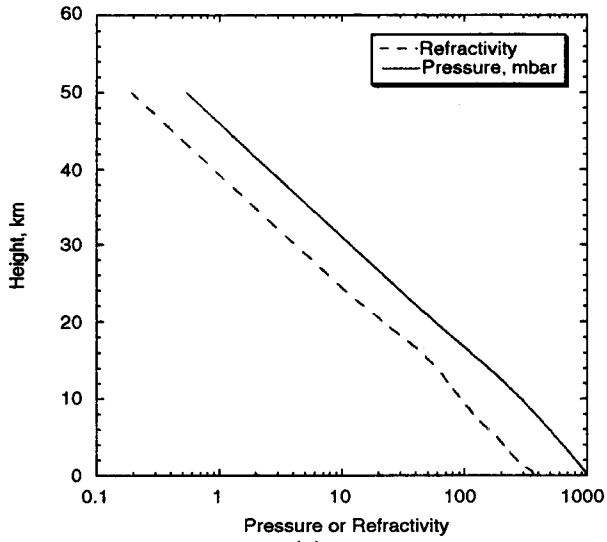
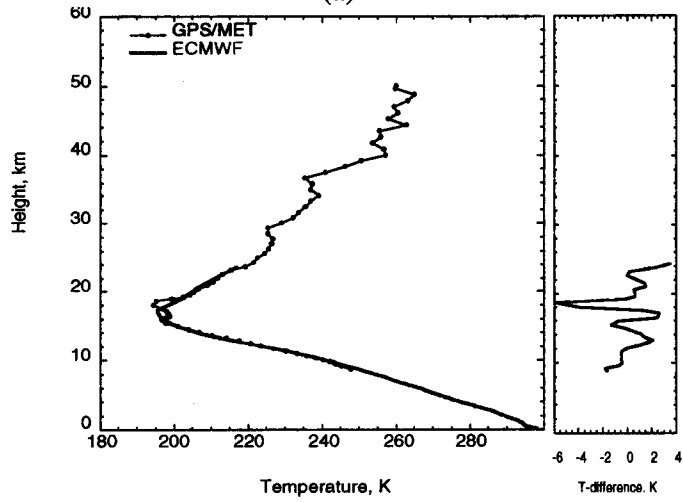


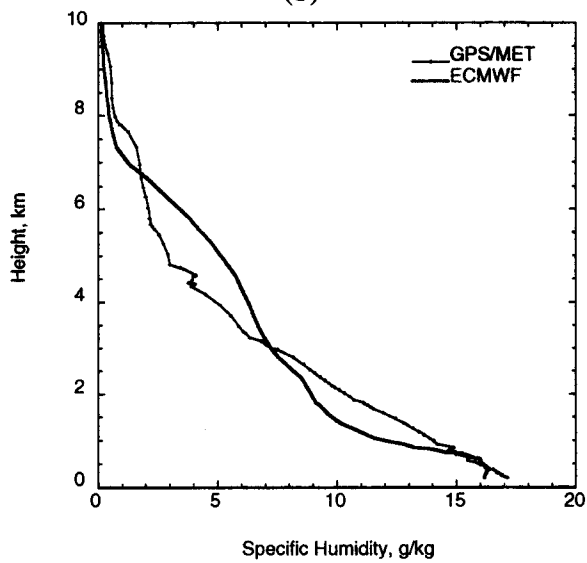
Figure 7: Estimated total atmospheric bending for L1 and L2, and ionospheric calibrated bending, as a function of a , the asymptote miss distance, for the occultation of Figure 2. At this stage of the processing, the height of the tangent point is not yet known, but can be approximated as ' a - radius of curvature' and is shown on the right scale.



(a)



(b)



(c)

Figure 8: (a) GPS/MET derived refractivity and pressure. The hydrostatic integral is started at 50 km altitude. (b) GPS/MET and ECMWF analysis temperatures (left) and their differences (right). The ECMWF highest level is at ~23km. The GPS/MET temperature is retrieved from 50 km down to ~8 km where $T=250\text{K}$. The agreement is better than 2K everywhere except near the tropopause, where we ascribe the discrepancy to the model due to insufficient resolution to capture the double tropopause detected from GPS/MET. (c) Specific humidity from GPS/MET and ECMWF analysis. In deriving the GPS/MET specific humidity, the ECMWF analysis temperature was used.

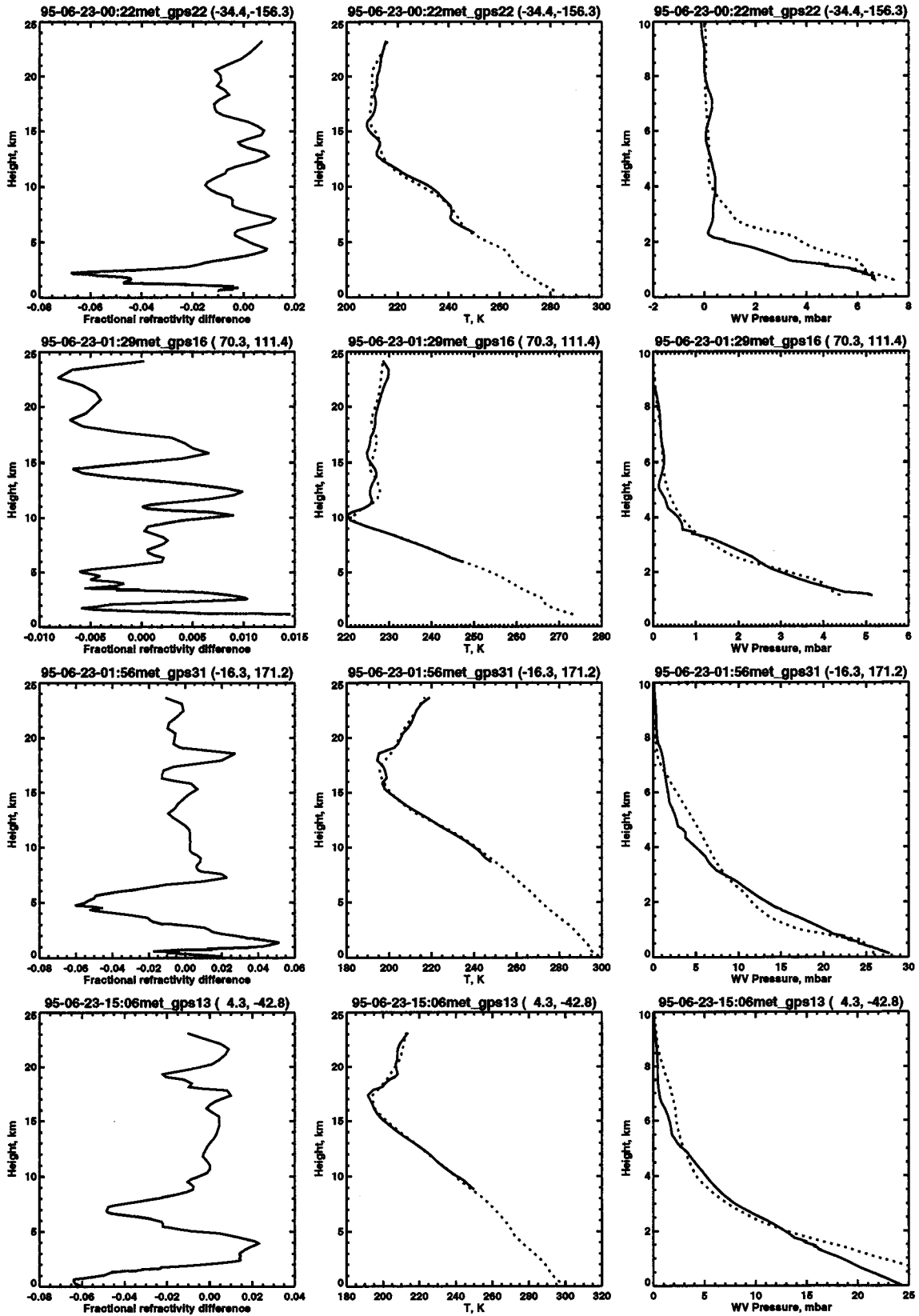


Figure 9: Retrievals of refractivity, temperature, and water vapor pressure (aligned horizontally for the same occultation) are shown for four different GPS/MET occultations. The date, time, occulting GPS, latitude and longitude of each occultation are indicated on the top of each plot. Retrieved parameters are compared to values derived from the nearest 6-hour ECMWF analysis interpolated to the location of the occultation. Fractional refractivity differences between GPS/MET and the analyses are shown on the left. GPS/MET temperatures and water vapor pressures are indicated in solid lines, those of the analysis are indicated in dashed lines. GPS/MET temperatures are shown only above the middle troposphere at a height where $T < 250\text{K}$.

Comparison of GPS/MET Retrievals to the ECMWF Model Summer AS-off Period

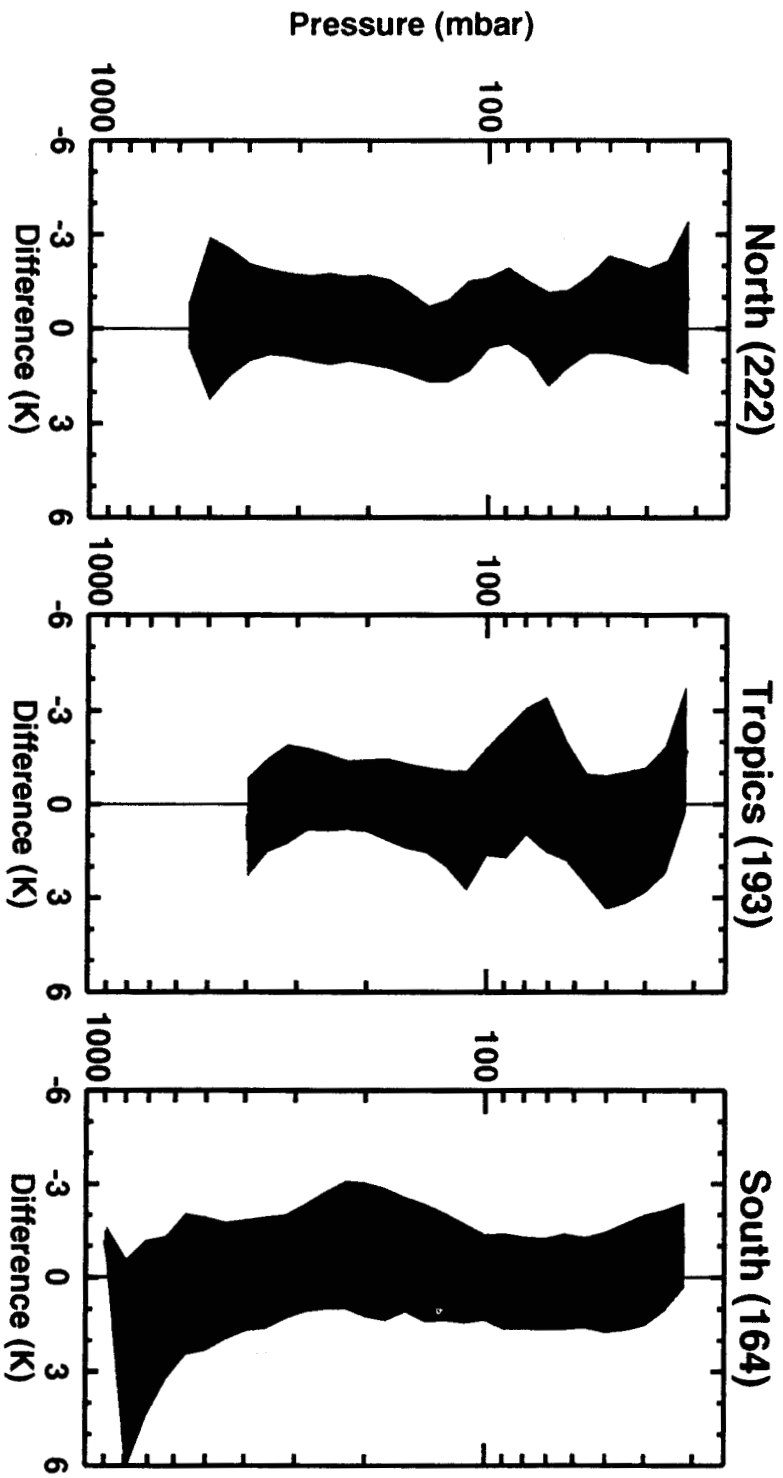


Figure 10: Statistical comparisons of temperatures derived from GPS/MET and the ECMWF analysis for the period June 21 to July 4, 1995. The comparisons is done for three regions: northern mid and high-latitude ($>30N$), tropical ($30S-30N$), and mid and high-southern latitudes ($>30S$). The number of occultations included in the statistics are indicated on the top of each panel.